



New Views of the Internal Structure of Planum Boreum from Enhanced 3D Imaging of Mars Reconnaissance Orbiter Shallow Radar Data

Nathaniel E. Putzig¹ , Frederick J. Foss II², Bruce A. Campbell³ , John W. Holt⁴, Matthew R. Perry¹ , Isaac B. Smith^{1,5} , Aaron T. Russell¹, Stefano Nerozzi⁴, Michael S. Christoffersen⁴, Isabella H. Mueller^{1,6,7}, and Paul C. Sava⁸

¹ Planetary Science Institute, Lakewood, CO 80401, USA; nathaniel@putzig.com

² Freestyle Analytical & Quantitative Services, LLC, Longmont, CO 80504, USA

³ Center for Earth and Planetary Studies, Smithsonian Institution, Washington, DC 20560, USA

⁴ Lunar and Planetary Laboratory, University of Arizona, Tucson, AZ 51555, USA

⁵ Lassonde School of Engineering, York University, Toronto, ON M3J 1P3, Canada

⁶ Columbine High School, Littleton, CO 80123, USA

⁷ Now at California Institute of Technology, Pasadena, CA 91125, USA

⁸ Department of Geophysics, Colorado School of Mines, Golden, CO 80401, USA

Received 2022 July 9; revised 2022 October 7; accepted 2022 October 12; published 2022 November 28

Abstract

We present first results from a new 3D radargram produced from 3399 Mars Reconnaissance Orbiter (MRO) Shallow Radar observations of the north polar region of Mars. While incorporating an additional 5 yr of observations relative to the prior 3D radargram, we employed surface-clutter simulations to improve the coregistration of the input data and thereby enhance the effective vertical resolution of features. Combining those improvements with the geometric corrections and an increase in signal-to-noise ratio afforded by the 3D imaging process, this data product provides new details about the interior of Planum Boreum, the Martian north polar cap. We assess the overall characteristics and compare portions of the new 3D radargram to results from prior studies that used either the prior 3D radargram or sets of 2D radargrams from individual MRO orbits. We find that the new 3D radargram has recovered essentially all of the vertical resolution inherent to the input data, and the increased coverage density has substantially reduced artifacts while enabling much greater detail in the imaging of subsurface layering and structures. These improvements extend throughout the 3D radargram, from the basal units to the shallowest subsurface layering in Planum Boreum, and out into the surrounding plains. Subsurface features such as a buried chasma, other layering structures and unconformities, and trough-bounding surfaces that offset shallow layering are now visible in unprecedented detail. A thorough analysis of this new 3D radargram and its implications for the geologic and climate history of Planum Boreum will extend over many years.

Unified Astronomy Thesaurus concepts: Mars (1007); Radar observations (2287); Polar caps (1273); Planetary climates (2184); Orbiters (1183); Planetary interior (1248)

1. Introduction

Planum Boreum, the broad dome that forms the north polar cap of Mars, sits atop the extensive plains of Vastitas Borealis that comprise much of the Martian northern hemisphere. The lower part of the cap consists of units that contain a variable mixture of water ice, dust, and sand, and they exhibit varying degrees of internal structure at outcrops and in radar sounding data (Nerozzi & Holt 2018). These basal units (BUs) are overlain by sequences of finely layered materials known as the north polar layered deposits (NPLDs) that have a high fraction (~95%) of water ice (Grima et al. 2009) and contain a host of structures such as layering packets and discontinuities (Phillips et al. 2008; Putzig et al. 2009; Holt et al. 2010; Smith et al. 2016), troughs in a spiral pattern that disrupt layers both at the surface and well into the interior (Smith & Holt 2010, 2015), surficial and buried chasmata (Holt et al. 2010), and surficial and buried impact craters (Putzig et al. 2018). The features observable at the surface and in the interior of the polar cap have long been viewed as a key to understanding climate cycles on Mars (Byrne 2009; Clifford et al. 2000; Smith et al. 2020),

and Planum Boreum has been a primary observing target for the Mars Reconnaissance Orbiter (MRO) and its Shallow Radar (SHARAD) sounder (Seu et al. 2007) since their arrival at Mars in 2006. While MRO is a US spacecraft operated by NASA through the Jet Propulsion Laboratory, SHARAD was contributed and is operated by the Italian Space Agency through the Sapienza University of Rome and has an international team of participants.

2D SHARAD radargrams are typically formed from sets of vertical subsurface-sounding pulse records (frames) created with synthetic aperture processing and arranged along the ground track to provide a cross-sectional view of radar reflections from the surface and subsurface. In real geologic settings, radar echoes do not come strictly from features directly below the spacecraft. Echoes recorded by an orbital radar system can arise from nadir and off-nadir surfaces that are oriented normally to the spacecraft. Off-nadir echoes are often called “clutter,” as they may confuse geologic interpretation of echoes that return subsequent to the surface reflection. While coherent or incoherent summing of data acquired along closely adjacent ground tracks will enhance the consistent reflections at nadir relative to clutter echoes that shift in time and frequency, such treatment does not provide the geometric reconstruction needed to properly position the surface and subsurface returns in regions with moderate and large-scale topographic relief.



Original content from this work may be used under the terms of the [Creative Commons Attribution 4.0 licence](https://creativecommons.org/licenses/by/4.0/). Any further distribution of this work must maintain attribution to the author(s) and the title of the work, journal citation and DOI.

In this work, we use a 3D imaging technique that was demonstrated previously by Foss et al. (2017) to place echoes from multiple SHARAD tracks into their appropriate spatial locations, which provides what is essentially a more accurate transformation from the delay-time and Doppler (azimuth-time) coordinates to real-world positions. This type of processing permits some degree of enhancement of the signal-to-noise ratio (S/N) by summing echoes from locations seen on multiple ground tracks, and it produces a 3D interpolated radar image for scientific analysis.

In Section 2, we provide an overview of the methods for producing this new 3D radargram and the techniques used in analyzing it. In Section 3, we present the resulting improvements of the new 3D radargram relative to the prior one along with several examples of the subsurface mapping advances that the new data volume enables when tracking features of Planum Boreum previously assessed using 2D single-orbit radargrams and the prior 3D radargram. In Section 4, we discuss future work enabled by the new 3D radargram and the implications for producing similar products for other locations on Mars.

2. Methods

2.1. 2D Radar Data Processing

Raw observations by SHARAD are in the form of single-pulse records that contain 3600 voltage measurements taken every $0.0375 \mu\text{s}$ over a $135 \mu\text{s}$ record. The vertical spatial resolution is the inverse of the 10 MHz chirp bandwidth, or 15 m in free space, and the time sampling records this signal at a free-space interval corresponding to 11.25 m (i.e., it is somewhat oversampled). In the radar processing by the US portion of the SHARAD team (Campbell & Phillips 2014, 2021), the output radargrams represent another twofold oversampling, so each vertical bin corresponds to 5.625 m in free space. For subsurface portions of the records, the spatial sampling is further enhanced as the square root of the real permittivity of the subsurface materials. It is important to note that the oversampling does not improve the ability of the radar to resolve geologic features beyond the limit imposed by the signal's bandwidth. In practice, processing of the data typically applies a windowing function to suppress sidelobes of signal peaks that are induced by the limited bandwidth, and this process has the side effect of coarsening the effective vertical resolution, largely offsetting the improvement provided by the higher permittivity of subsurface materials. For example, nearly pure water ice such as that which makes up the NPLDs has a real permittivity of ~ 3 , yielding a nominal range resolution of 8.7 m, but the Hann filtering applied broadens the signal by a factor of ~ 1.6 , yielding an effective range resolution in ice of 14 m.

Basic SHARAD processing uses the delay-Doppler implementation of synthetic aperture radar (SAR), compensating for the delay and frequency history of observations of a single point to sum over a number of along-track observations. The primary parameters in this processing are the duration of the synthetic aperture and the number of frequency-resolution cells around the nadir point chosen for multilook averaging. Based on examples in the US SHARAD processing document in the Planetary Data System (PDS; Figure 3 of Campbell & Phillips 2014), we selected a synthetic aperture length double (17.55 s, or 60 km along the spacecraft ground track) that of the standard PDS products (8.774 s) to highlight sloping surface features.

This choice of aperture duration results in the imaging of surface and subsurface reflectors over a greater range of slope, but it sacrifices about a factor of 60% (4 dB) in echo S/N for a flat, horizontal surface. We made that trade assuming that proper spatial placement of the echo power from each pulse leads to sufficient incoherent summation improvement to offset much of the 4 dB S/N loss in the output radargram frames. This assumption is tested in Section 3.1.

Standard processing also includes compensation for ionospheric phase distortion effects, which were documented by Campbell et al. (2011, 2014). For the 3D work, we implement a finer along-track spacing and more rigorous fitting algorithm for the derivation of correction factors, improvements now also included for US SHARAD products in the PDS. The phase derivation method includes an estimation of variable range (vertical) delays induced by the ionosphere, which are then removed in subsequent processing. In the prior work, Foss et al. (2017) found that small but pervasive range delays remained between the frames of the 2D radargrams going into any given location within the 3D binning grid. These residual delays led to a twofold loss of effective vertical resolution in the 3D radargram relative to that provided by the input 2D radargrams.

To limit the impact of these residual ionospheric delay errors, we introduced a new processing step wherein the frames of each input 2D radargram are adjusted in delay time such that the first arrivals from the surface match (as defined by a cross-correlation operator) those of a surface-clutter simulation produced from a digital elevation model (DEM) of the Martian surface (Choudhary et al. 2016). For the DEM, we merged the 128-pixel-per-degree surface from the Mars Global Surveyor (MGS) Mars Orbiter Laser Altimeter (MOLA) mission experiment gridded data records (Smith et al. 2003) with a surface determined from the prior 3D radargram in the annulus between the highest northern latitudes reached by the MRO and MGS spacecraft (Putzig et al. 2018).

The remaining essential 2D processing steps (Foss et al. 2017) were as follows.

1. Convert data values from power to reflection strength (the square root of power) for consistency with expectations of the seismic data processing and analysis codes being employed.
2. Redatum the 2D radargrams that were coregistered to clutter simulations to their respective orbital acquisition datums by restoring appropriate along-track time delays.
3. Demigrate the 2D radargrams (now referenced to the spacecraft orbit) to approximately reverse the along-track range migration performed during SAR processing.
4. Redatum the demigrated radargrams to a common average orbit radius (3692.4796 km) and, for storage and computational efficiency, retain only the data within a $135 \mu\text{s}$ range window below the maximum areoid radius (3396.3830 km) within the region spanned by the entire set of 2D radargrams to be used in the 3D processing (note that the areoid datum is entirely above the north polar surface).

2.2. 3D Radar Data Processing

We performed 3D processing using data from 3399 2D radargrams prepared as described in Section 2.1. The essential 3D processing steps (Foss et al. 2017) were as follows.

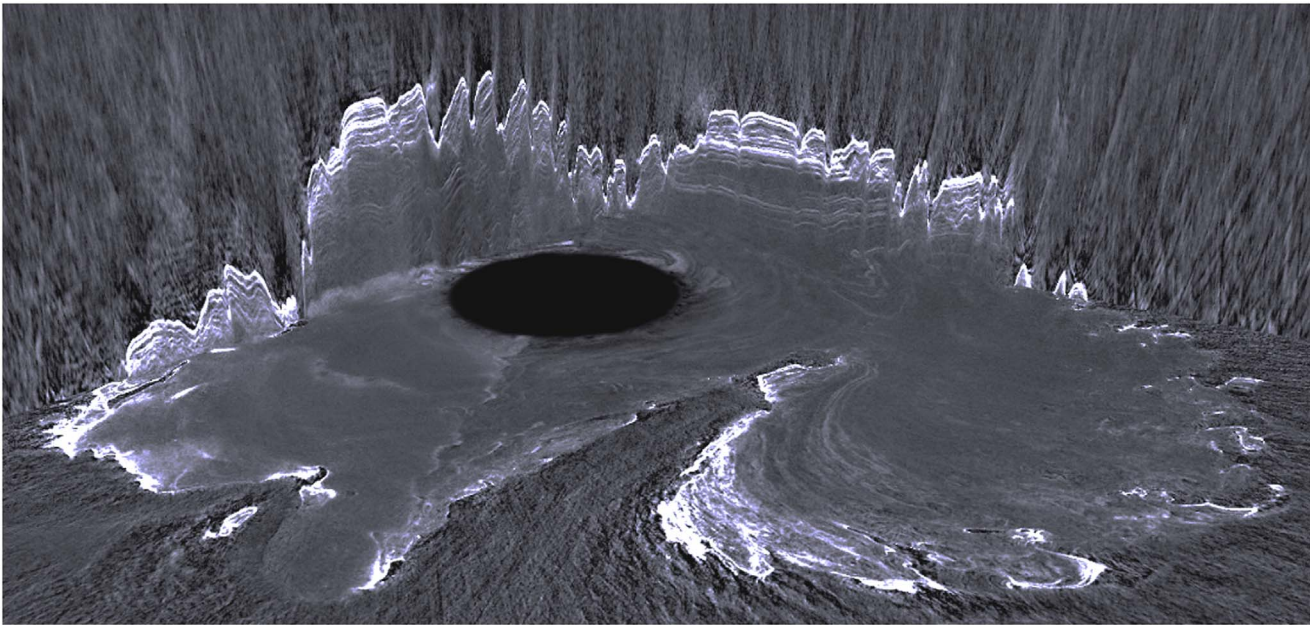


Figure 1. Perspective view of the interior of Planum Boreum. This cutaway view consists of three orthogonal slices through the depth-converted PB3Dv2 radargram (inline 3405 in the upper right, crossline 3062 in the upper left, and horizontal slice at -3142.5 m elevation in the lower half of the image) and looks toward 150°E . The black circle in the middle is centered on the north pole with a diameter of 300 km and constitutes a no-data zone due to the $2^\circ33'$ offset of the MRO orbit from the pole. Scales vary in this view, which shows the upper ~ 2 km of the ~ 1200 km wide Planum Boreum at a vertical exaggeration of 150:1.

1. Create 3D-geometry and processing-parameter databases along with a spatial binning grid (matching that of the previous work) and assign this information to each frame included in the 3D volume based on its location within the spatial binning grid.
2. Remove any lingering delay-time misalignments (as determined via cross-correlation) between frames contributing to each spatial bin.
3. Sum together frames contributing to each spatial bin after applying appropriate weights to frames from different observations to remove gain variations introduced by differences in the orientations of MRO's solar array and high-gain antenna during acquisition (Campbell et al. 2021).
4. Interpolate existing frames within the 3D summed volume to populate spatial bins without contributions, thereby regularizing the data. Equatorward of the SHARAD no-data zone (latitudes $>87.4^\circ\text{N}$), 56% of bins required infilling across the entire 3D-imaged region that extends down to 60°N . However, only 18% of bins required infilling within the latitudes of the NPLDs' SHARAD coverage (between 80°N and 87.4°N).
5. 3D downward continue (Biondi et al. 2006; Levin & Foss 2014) the interpolated and regularized summed volume from its common orbit radius datum to the maximum areoid radius datum (properly accounting for the windowing mentioned in Section 2.1, step 4). This step has the effect of focusing the image as if the data were recorded much closer to the surface.
6. 3D migrate (Stolt 1978) the downward-continued volume to image the data at reflection/scattering locations rather than (downward-continued) recording locations.
7. Convert the migrated volume from delay time to depth below the maximum areoid radius assuming free space velocity above and pure water-ice velocity below the DEM surface discussed in Section 2.1. Where higher

- permittivity (and thus lower velocity) exists in portions of Planum Boreum (i.e., zones such as BUs that may have higher fractions of non-ice material), thicknesses will be overestimated by a factor of the difference in the reciprocals of the square roots of permittivities. Given the potential horizontal variability of velocity, such overestimation may result in geometric distortions such as the incomplete flattening of a horizontal interface.
8. Change the datum of the migrated depth volume from the maximum areoid radius to 10,125 m above the MOLA areoid to match the datum of the standard US 2D radargrams.

2.3. 3D Radar Image Analysis

2.3.1. Radiometric Analysis

To enable radiometric comparisons (Section 3.1.2), we selected data for a small area in the topographic saddle region where Gemina Lingula meets the main lobe of NPLDs from four data sets: PDS standard US reduced data record (RDR) 2D data products (Campbell & Phillips 2014, 2021), long-aperture 2D data products (Section 2.1), the original Planum Boreum 3D data product (Foss et al. 2017), and our enhanced Planum Boreum 3D data product (Section 2.2). We selected this region due to its relatively smooth topography and minimal off-nadir returns, which allowed for more direct comparisons between the data sets. After extracting the reflection strength of the surface returns from each data set and converting to power, we binned the results into 1 dB bins from -50 to 0 dB.

2.3.2. BU Analysis

The Geophysics by SeisWareTM (GSW) software provides profile analysis tools for use with cross-sectional views of 3D data sets, and we used these tools to map the lateral extent and geometry of a reflector within the cavi geologic unit

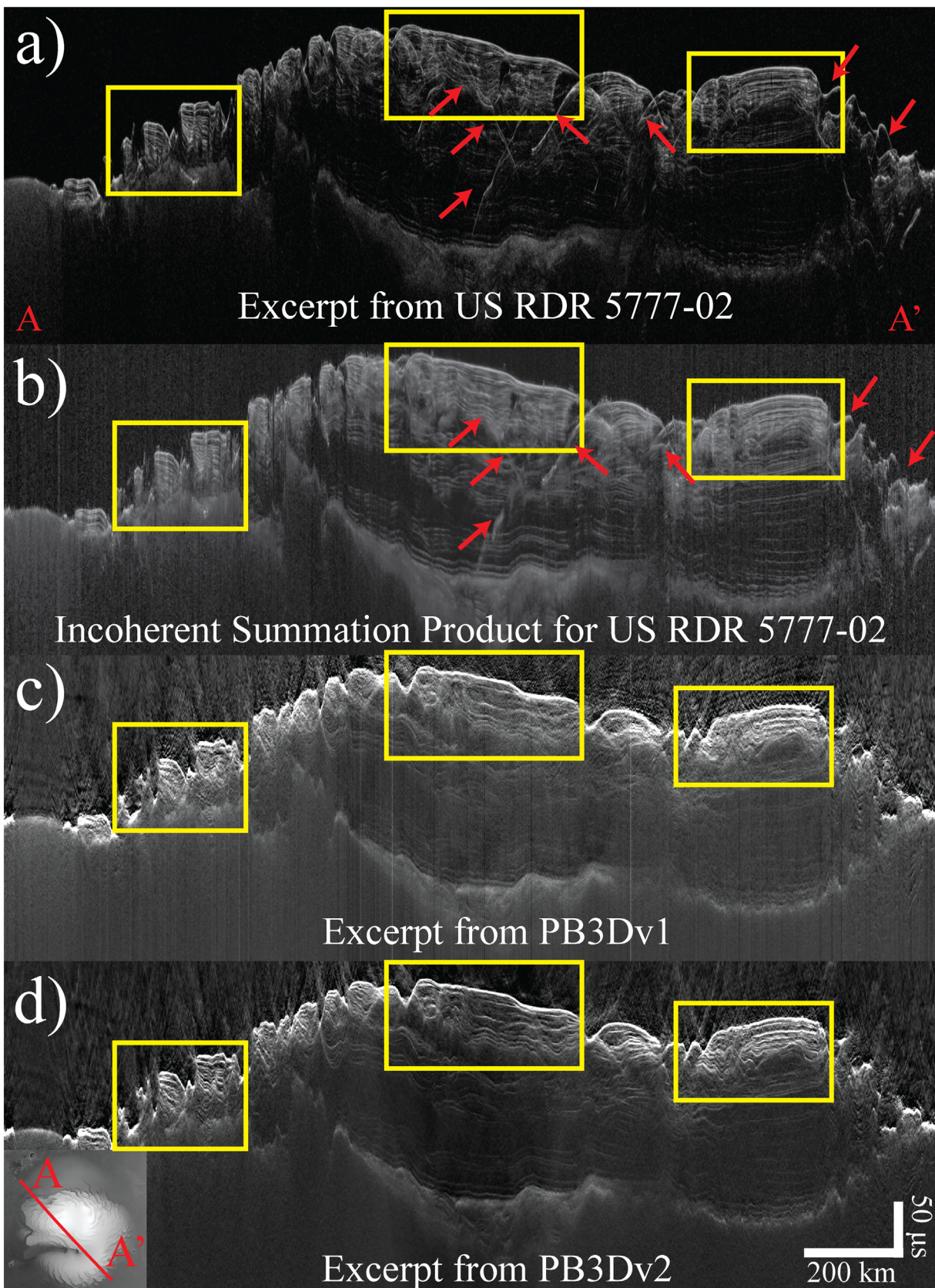


Figure 2. Comparison of features in 2D and 3D radargrams. (a) US RDR 2D radargram for observation 5777-02. (b) Incoherently summed 2D radargram along the track of observation 5777-02. (c) Profile excerpted from the PB3Dv1 radargram along the track of observation 5777-02. (d) Profile excerpted from the PB3Dv2 radargram along the track of observation 5777-02. For each panel, the power is displayed in grayscale such that the highest powers are white and lowest powers are black. The vertical axes are in two-way travel time. Red arrows point to examples of clutter in the 2D radargrams that are cleared up in the 3D radargrams. Yellow boxes draw attention to zones of differences in resolution and geometric distortion between the panels. The inset in panel (d) shows the location of the 2D radargram track along A–A' across Planum Boreum in MOLA shaded relief.

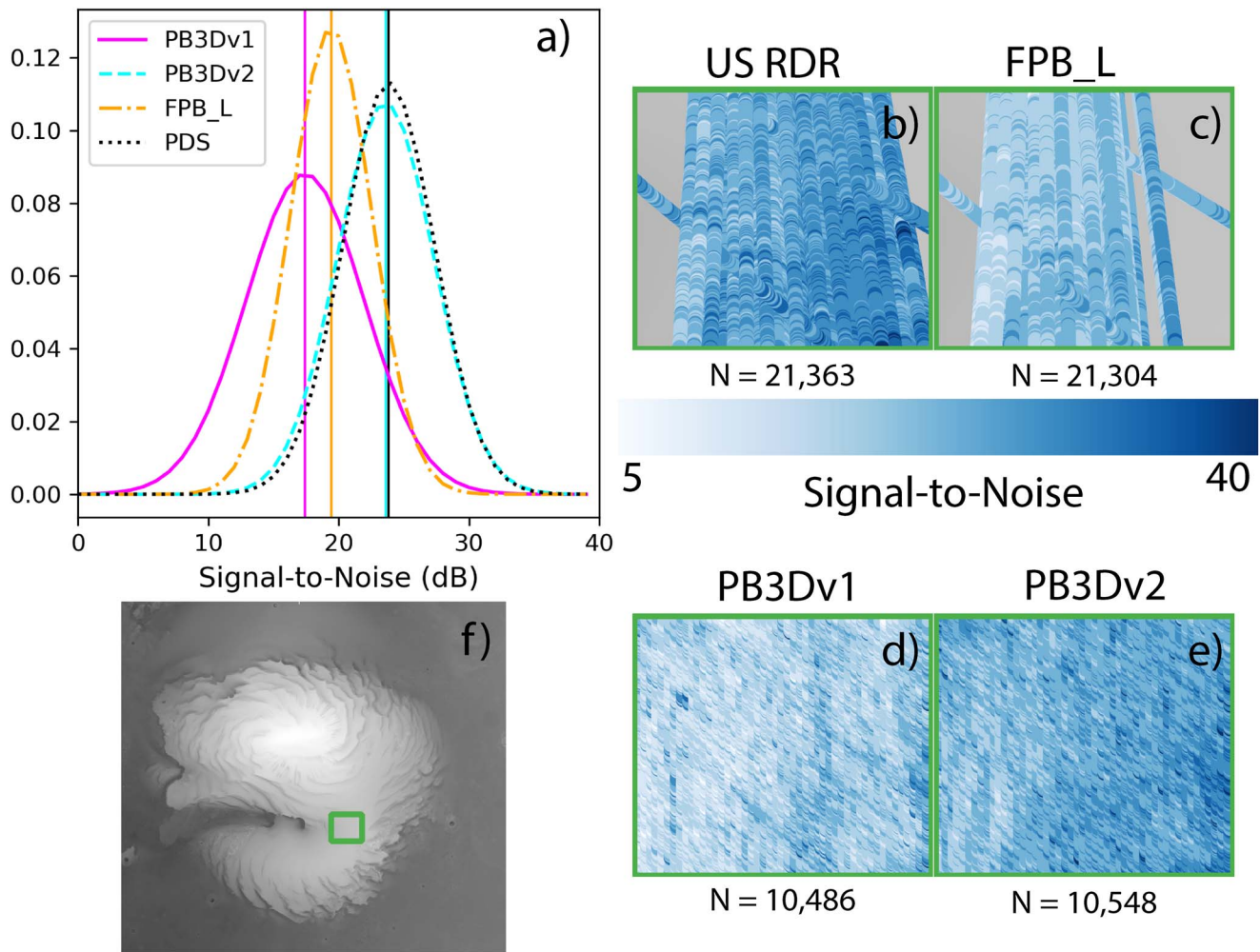


Figure 3. Radiometric analysis of SHARAD data. (a) Gaussian fits to histograms of S/N. Histograms correspond to the analyzed PDS radargrams (dotted black; panel (b)), L2D radargrams (dotted–dashed orange; panel (c)), PB3Dv1 radargram (solid magenta; panel (d)), and PB3Dv2 radargram (dashed cyan; panel (e)). Each histogram is presented with its mean value (vertical lines in panel (a)) within the Gemina Lingula region of interest (panel (f); green box).

Table 1
Radiometric Analysis Results

Data Set	Surface Power Return		Noise Power Return		S/N	
	Mean	StDev	Mean	StDev	Mean	StDev
L2D	-6.12	0.01	-1.71	0.75	-4.41	0.41
PB3Dv1	-8.80	0.26	-2.51	-0.66	-6.41	-1.00
PB3Dv2	-6.48	0.32	-6.26	-0.27	-0.24	-0.18

Note. Power values and S/N are presented in dB within the radiometric study area (see Figure 3) relative to the US RDR products available on the PDS of the long-aperture 2D radargrams and the 3D radargrams. For the US RDR products, the mean surface power return is estimated to be -17.88 ± 2.60 dB, and the mean S/N is $\sim 24 \pm 6$ dB (see Figure 3(a)).

(Tanaka & Fortezzo 2012) just below the surface in Olympia Planum in the new data volume. Due to the limited time for analysis, we extracted the peak strength of the reflector on every 10th inline and crossline to form a grid (where inline and crossline profiles are taken along the X and Y dimensions of the 3D binning grid). This reflector is visible in a few of the original SHARAD 2D radargrams, but it has not been mapped previously, likely due to the unfavorable geometry of the orbit tracks.

Using the same inline and crossline grid-mapping approach, we delineated a reflector within the cavi unit in Planum Boreum that was mapped in SHARAD 2D profiles by Nerozzi et al. (2022) and interpreted as the contact between the cavi and rupēs geologic units (Tanaka & Fortezzo 2012). We then compared the extent of our mapping to the previous map of this contact.

2.3.3. NPLD Stratigraphic and Structural Analysis

We used the GSW software to perform an analysis of a set of surface-conformal reflectors that are identifiable within the uppermost part of the new Planum Boreum 3D radargram (PB3Dv2). We mapped a radar-bright reflector near the top of that stratigraphic sequence that can be confidently traced across much of the NPLDs. In previous work, this reflector was mapped as the base of a widespread recent accumulation package (WRAP; Smith et al. 2016). We then compared our results to that previous mapping of the WRAP within the area of overlap.

In addition, we mapped several radar-bright reflectors in the uppermost stratigraphic sequence within the central region of Gemina Lingula. We chose subsurface reflectors to map based on their high power and their conformability with the surface reflector and each other.

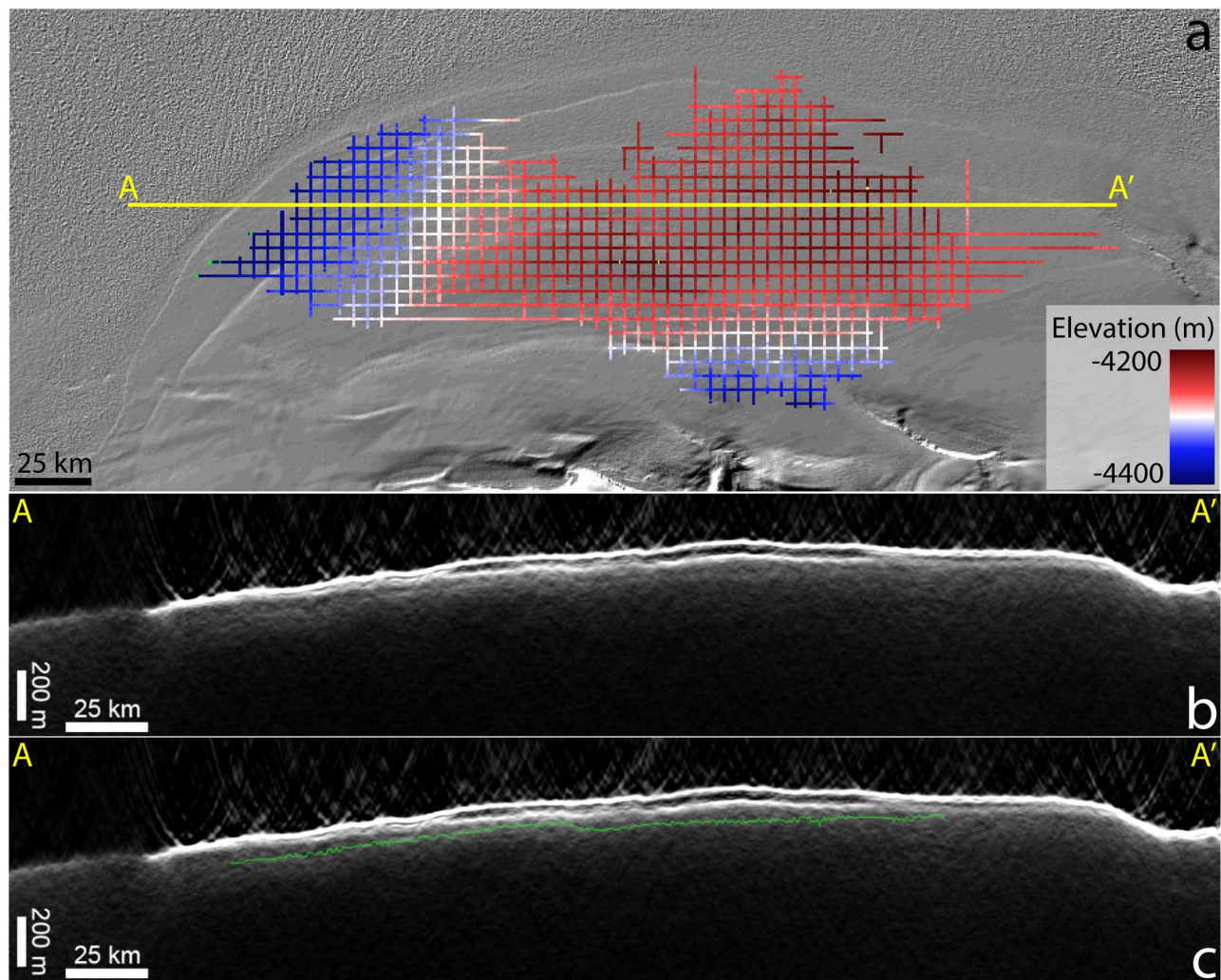


Figure 4. Cavi unit internal reflector in Olympia Planum. (a) Elevation (colors) of the cavi unit internal reflector mapped in Olympia Planum using the PB3Dv2 depth-corrected radargram. We mapped the reflector every 10 inlines and every 10 crosslines, thus forming the grid shown over the MOLA shaded relief base map. The A–A' line is the location of the profile extracted from the 3D radargram as displayed in the following panels, which show views wherein the relatively faint reflector is (b) uninterpreted and (c) interpreted (green line).

Using the reflector mapping methods described above, we also revisited the geometry of the lowermost NPLD-wide angular unconformity described by Putzig et al. (2009) and Holt et al. (2010). Given the broad lateral extent of this surface and limited time, we expedited the analysis by mapping reflectors every 20th inline and crossline. The NPLD internal reflectors rarely cross each other along the unconformity, but their geometry still makes the location of the contact easy to delineate. The angular unconformity extends laterally into a disconformity that we mapped by extracting the peak amplitude of the closest reflector. The resulting map was then compared to that of Holt et al. (2010).

2.3.4. Spiral Trough Analysis

Similar to other methods, we employed GSW to extract transects from the data volume crossing spiral troughs (Tanaka & Fortezzo 2012). We selected five reflectors that are stratigraphically high enough to encounter the bounding surfaces of the spiral troughs at depth, and we traced them over hundreds of kilometers through the data volume. One of those reflectors is the WRAP unconformity (Smith et al. 2016), and in this portion of the s, the unconformity appears as a bright reflection. We selected two transects of the data volume that run nearly perpendicular to the

spiral troughs, and we chose another six transects that cross the first two, with the purpose of demonstrating that each of the five reflectors are contiguous across all parts of the region of interest. At each location that intersects a spiral trough, Smith & Holt (2010, 2015) noted that a discontinuity is present, making it difficult to track the reflectors. To trace reflectors around those discontinuities, Smith & Holt (2015) employed a series of intersecting 2D tracks at great expense of time and effort. Using the 3D radargram, mapping around the spiral trough discontinuities takes only a few minutes.

3. Results

In this section, we describe results from the analysis of PB3Dv2, comparing them to those achieved previously with single-orbit 2D radargrams and the first Planum Boreum 3D radargram (PB3Dv1).

3.1. 3D Radar Imaging Results

3.1.1. Imaging Improvements

The efforts to improve the 3D radar imaging of the interior of Planum Boreum as described in Sections 2.1 and 2.2 were

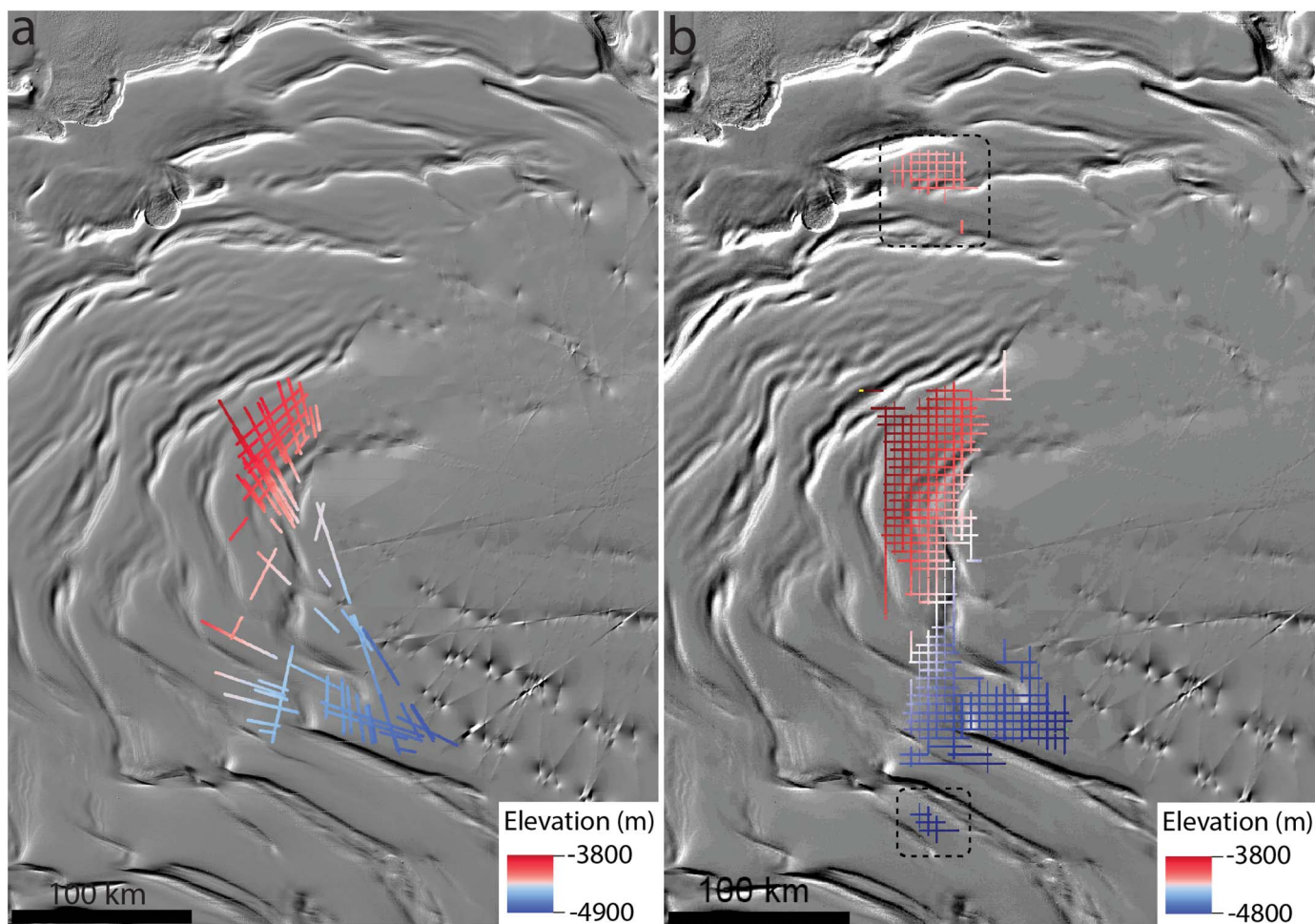


Figure 5. Contact between the rupēs and cavi units. (a) Extent and elevation of the reflector mapped by Nerozzi et al. (2022) using SHARAD 2D radargrams and interpreted by them as the possible contact between the rupēs and cavi units. (b) Same reflector mapped in a 10×10 line grid using the new depth-corrected 3D radargram. Note the denser and more continuous mapping across the spiral troughs and the detection of the same reflector in two new separate regions (black dashed boxes). The base map is MOLA shaded relief.

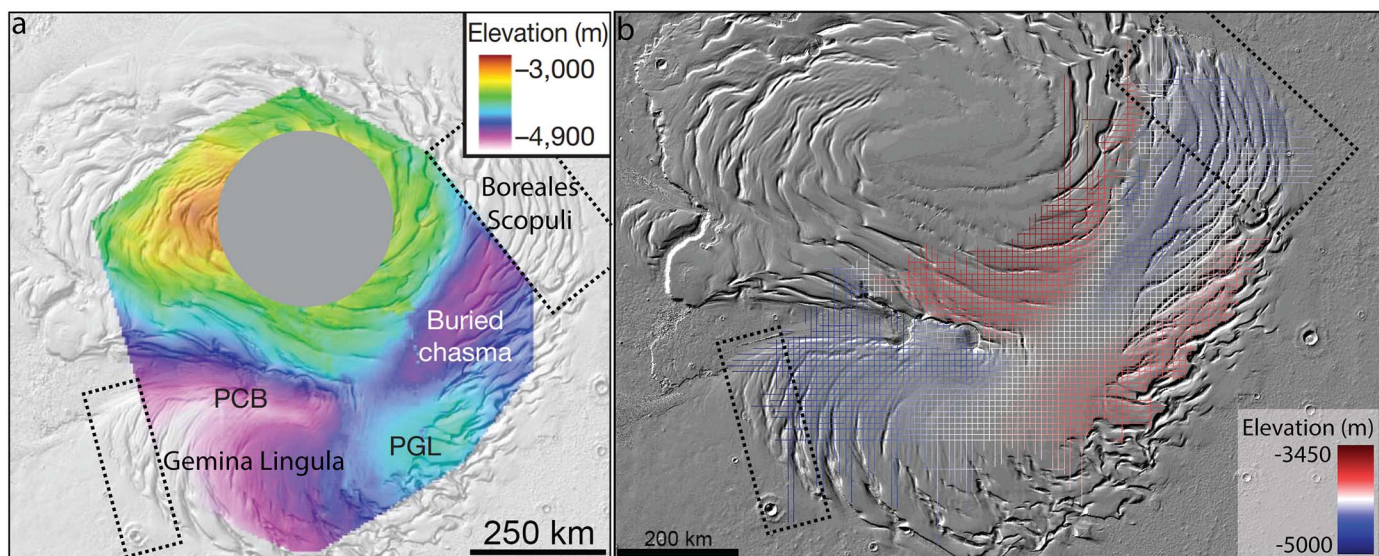


Figure 6. Revised mapping of the lower NPLD unconformity. (a) Elevation map of the lower unconformity in the NPLDs from Holt et al. (2010), where “PCB” indicates the location of paleo-Chasma Boreale, and “PGL” is paleo-Gemina Lingula. (b) Inline and crossline grid map of the same unconformity from this study. Note the newly mapped areas in the high-relief regions of Boreales Scopuli and southwestern Gemina Lingula (black dotted boxes). The base maps are MOLA shaded relief.

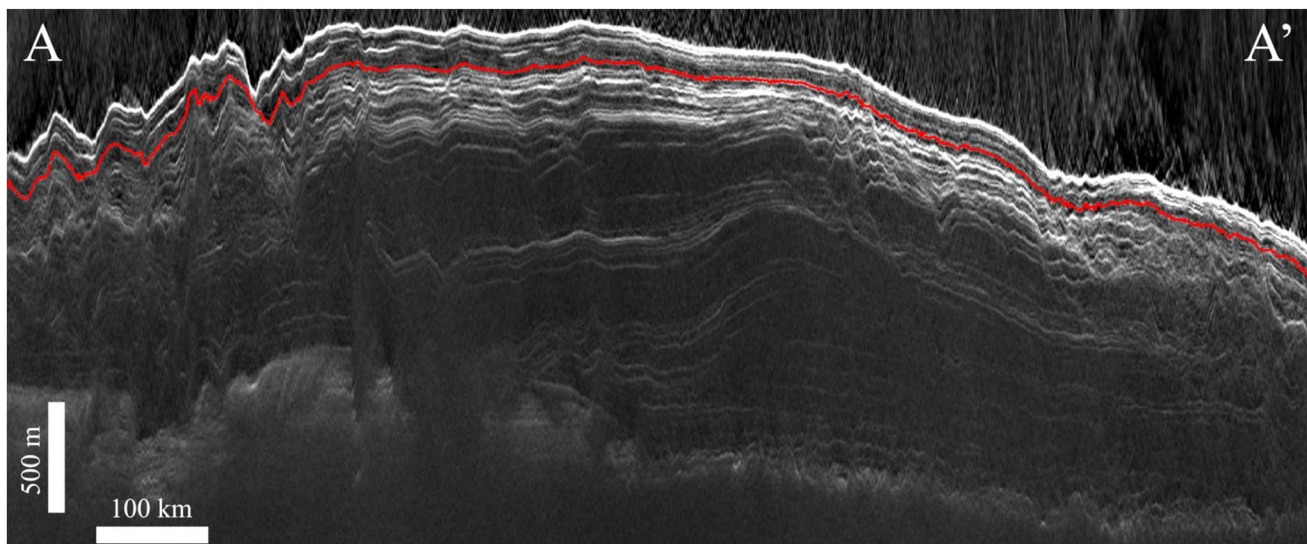


Figure 7. Upper NPLD unconformity. Profile A–A’ extracted from the new depth-converted 3D radargram extends across the main lobe of the NPLDs and Gemina Lingula. The WRAP base is shown by the red line. See Figure 8 for the profile transect path.

generally very successful. The vast majority of residual time delays between crossing 2D radargrams were removed, enabling a nearly complete retention of the original vertical resolution and an improvement in the repositioning of clutter throughout the data volume. The increase of 48% in the number of included 2D radargrams also contributed to the improved imaging and S/N relative to the prior volume while improving the effective spatial resolution at lower latitudes. Figure 1 illustrates the overall extent and scale at which layering can be resolved within this new 3D radargram.

In Figure 2, we present an example of imaging improvements seen for a single profile across Planum Boreum. A SHARAD 2D observation (5777-01) taken on a single pass of MRO over the region (Figure 2(a)) crosses areas of the polar cap with numerous surface troughs, as well as some relatively smooth and flat-lying areas. As noted in the figure, the varying topography produces numerous off-nadir returns (clutter signals), which often obfuscate subsurface returns from below the nadir track, making it difficult to ascertain subsurface structure along the profile. By summing data along the track of this observation together with that taken from all crossing observations in an incoherent manner (Whitten & Campbell 2018), we produced an enhanced 2D radargram (Figure 2(b)) that improves S/N and partly suppresses clutter without repositioning it. After applying the 3D imaging process described in Section 2.2, the clutter is further mitigated, and other geometric distortions are corrected such that the layering geometries are more clearly represented (Figure 2(c)). Steps taken in the latest 3D imaging project to remove residual timing delays and include additional data have further sharpened the image (Figure 2(d)). While the 2D incoherent-summing method yields a distinct S/N improvement, most notably in the deeper subsurface, the 3D processing maintains a broader overall dynamic range.

3.1.2. Radiometric Assessment

We compare the power (dB) of the surface return for standard US SHARAD RDR 2D (US RDR) radargrams in the PDS, the long-aperture 2D SHARAD (L2D) radargrams used as input data to the 3D imaging, the previous version of the 3D radargram (PB3Dv1), and the new version (PB3Dv2) within the saddle region of Gemina Lingula (Table 1 and Figure 3).

This region was chosen due to its being relatively flat and displaying very few off-nadir returns within the 2D radargrams, thereby offering an ideal location in which to make a fair comparison between the different data sets. The surface power returns were extracted from the various data sets, and Gaussian fits to their S/N histograms were compared. For calculating S/N, the noise level is measured 10 μ s above the surface return.

In the region of interest, the US RDR radargrams have an average S/N of \sim 24 dB. As mentioned above, the long-aperture data set (L2D) used for 3D imaging has \sim 4 dB loss (\sim 19 dB) in S/N compared to the US RDR products. The preprocessing and imaging steps employed during the creation of the PB3Dv1 radargram not only were unable to recover this S/N loss, they actually lost an additional 2 dB compared to the input data sets for an S/N of \sim 17 dB. However, the improvements made during the creation of the PB3Dv2 radargram enabled the recovery of the original S/N.

While the PB3Dv2 radargram recovers the S/N of the US RDRs, it is also important to note that the imaging of the PB3Dv2 radargram is greatly improved in more topographically complex regions due to the repositioning of the clutter to its point of origin (e.g., Figure 2).

3.2. Planum Boreum Internal Features

3.2.1. Basal Units

Using SHARAD 2D radargrams, Nerozzi & Holt (2019) showed that the cavi unit contains several reflectors that extend laterally for tens to hundreds of kilometers, and they interpreted those reflectors as evidence of alternating water-ice and eolian sand sheets. However, the presence of surface and subsurface clutter and unfavorable 2D profile geometry made mapping of cavi unit reflectors very difficult in some regions, including Olympia Planum and the innermost reaches of Planum Boreum. The 3D processing of the SHARAD volume presented in this study addresses all of these issues and allows for mapping along any arbitrary profile.

We mapped a reflector internal to the cavi unit in Olympia Planum, finding that it extends \sim 300 km in the E–W direction and \sim 150 km in the N–S direction (Figure 4). The reflector is mostly horizontal, except for gentle downward slopes in its northern and

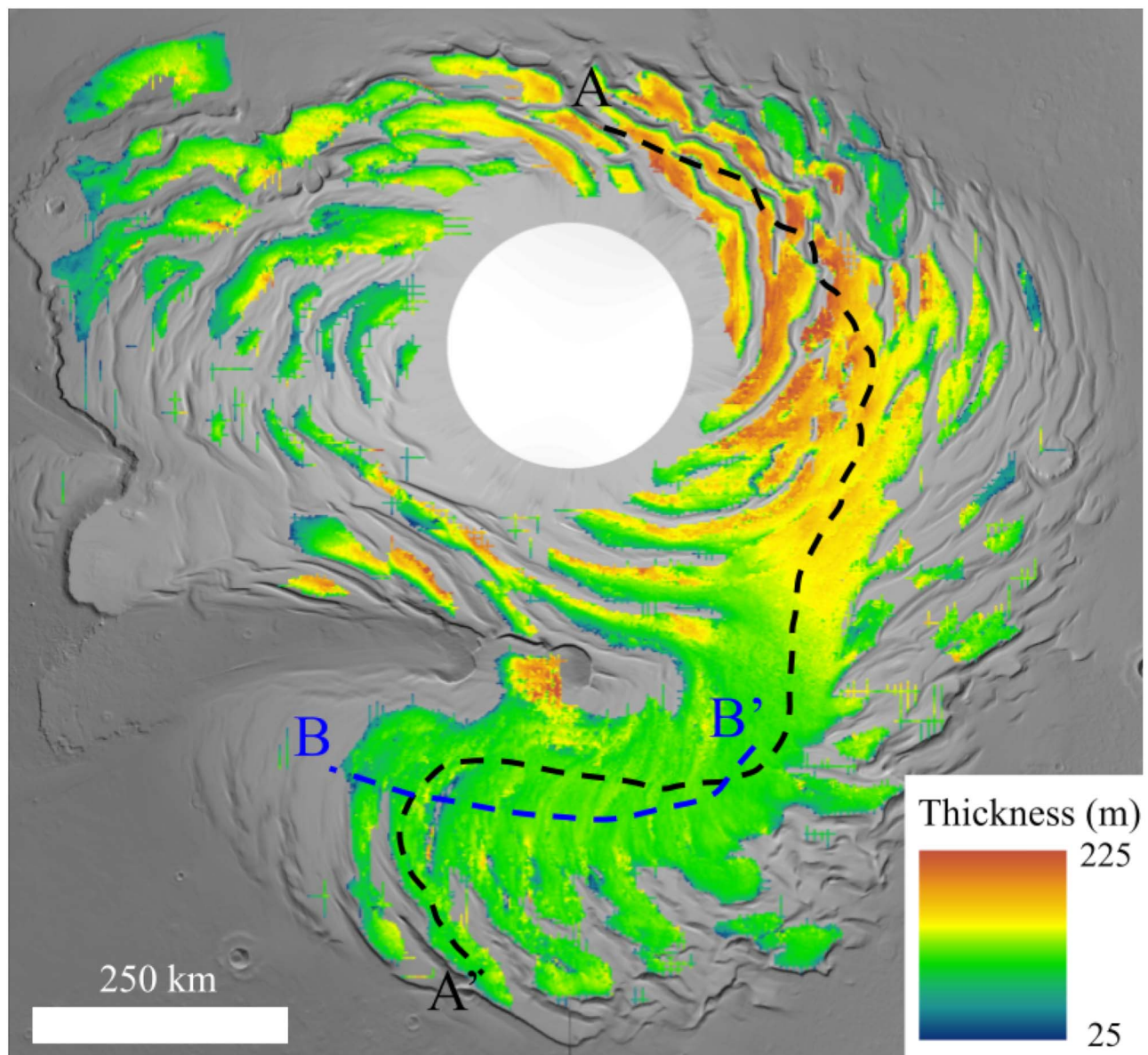


Figure 8. Revised map of WRAP thickness in the NPLDs using the new 3D radargram. WRAP is the uppermost section of the NPLDs above a regional unconformity. Black and blue dashed lines labeled A–A' and B–B' delineate the profiles extracted from the data volume as shown in Figures 7 and 9, respectively. The base map is MOLA shaded relief.

eastern reaches (blue and white areas in Figure 4(a)). The large lateral extent makes this reflector one of the most extensive within the cavi unit (Nerozzi & Holt 2019; Nerozzi et al. 2022).

The new data volume allowed us to greatly expand the mapping of the reflector first delineated by Nerozzi et al. (2022) and interpreted by them as the contact between the cavi and rupēs units (Figure 5). In particular, we found that the contact can be traced further to the southeast toward Gemina Lingula and that a similar reflector appears toward the southwest close to Olympia Cavi. Further mapping of this contact in the new 3D data set can inform us of the respective volumes of the two units, in turn constraining the amount of volatiles and lithic fines stored in the BUs.

3.2.2. Deep NPLDs

The lowermost section of the NPLDs is marked by a prominent angular unconformity first delineated by Putzig et al. (2009)

and mapped in more detail by Holt et al. (2010), who found that the unconformity forms the basal surface of a deep erosional chasma buried underneath younger NPLD layers. Beyond the buried chasma, the unconformity follows the flanks of Chasma Boreale and continues into a disconformity across other locations in the NPLDs. Thanks to the arbitrary profile geometry and orientation available for viewing transects of the new 3D radargram, we were able to extend the mapping of the unconformity and associated disconformity across Boreales Scopuli and southwestern Gemina Lingula (Figure 6). These regions are very dense in spiral troughs and steep scarps that prevented radar reflector mapping in previous efforts. We find that the buried chasma widens under Boreales Scopuli and reaches the base of the NPLDs. Similarly, the unconformity along Chasma Boreale becomes wider underneath Gemina Lingula in the southwest direction.

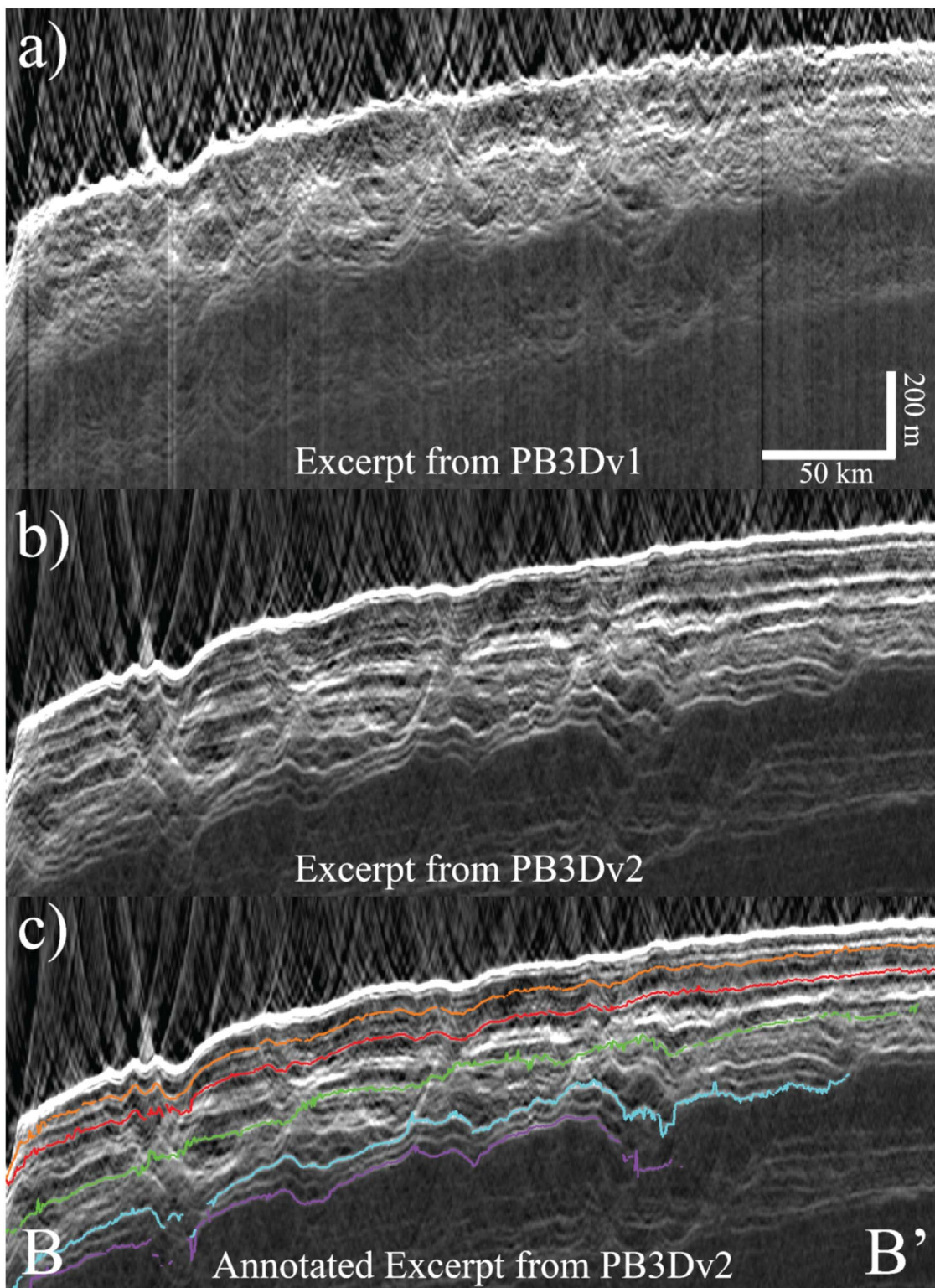


Figure 9. Gemina Lingula shallow layering. Profile B–B' is shown from the (a) original and (b) new depth-converted 3D radargrams, and panel (c) shows the five reflectors that were mapped across Gemina Lingula. The B–B' in Figure 8 shows the profile transect path. Lower mapped reflectors show structure that differs from that of upper layers, especially at buried troughs. Colored lines represent interfaces mapped by Mueller et al. (2021). The red line (second interpreted reflector below the surface) corresponds to the WRAP base.

3.2.3. Shallow NPLDs

Previous investigations have described the WRAP as an upper stratigraphic package that truncates lower reflectors (Smith et al. 2016). In our analysis using PB3Dv2, we find that the WRAP truncates deeper reflectors in several regions, most

notably in Gemina Lingula and around the margins of the main lobe of the NPLDs. However, we find that across the majority of the NPLDs, deeper reflectors are generally conformable to the WRAP (Figure 7), the base of which thus represents a disconformity over much of its extent. Our mapping of the

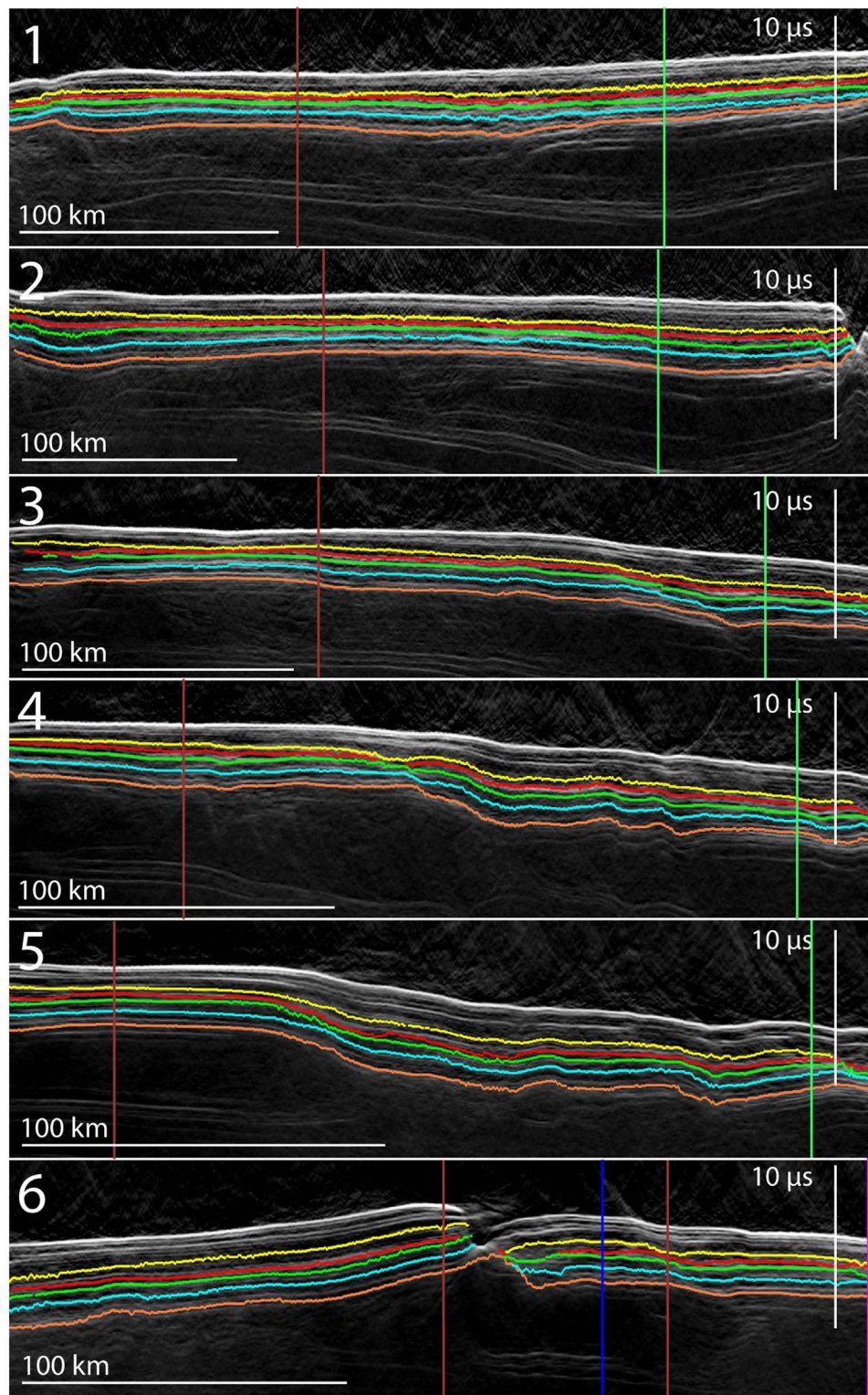


Figure 10. Correlation of reflectors around spiral troughs. Eight profiles extracted from the new 3D radargram highlight layering between and beyond the spiral troughs. Each profile is taken along the corresponding numbered and colored lines shown in the base map. Profiles 1–5 all tie to profile 7. Thus, it is possible to track stratigraphy across the troughs in profile 8, where it would be otherwise impossible to say with certainty that the reflectors were identical without numerous (order 50–100) 2D tracks to “zigzag” along a trough between tie points. Profile 6 does not tie to profile 7, so pattern matching is required to connect the trough it crosses to the others. The base map is cropped from an HRSC mosaic (Neukum et al. 2004). Colored vertical lines on each profile represent the tie points to crossing profiles, with colors corresponding to those of the tracks on the base map.

WRAP (Figure 8) is more limited geographically than that done previously by Smith et al. (2016) and resulted in an estimated ice volume of $\sim 7000 \text{ km}^3$. Masking the previous mapping of

the WRAP to the geographical extent of our work for a direct comparison, we find that our estimated ice volume is consistent with the previous work, with only a 2% increase in the

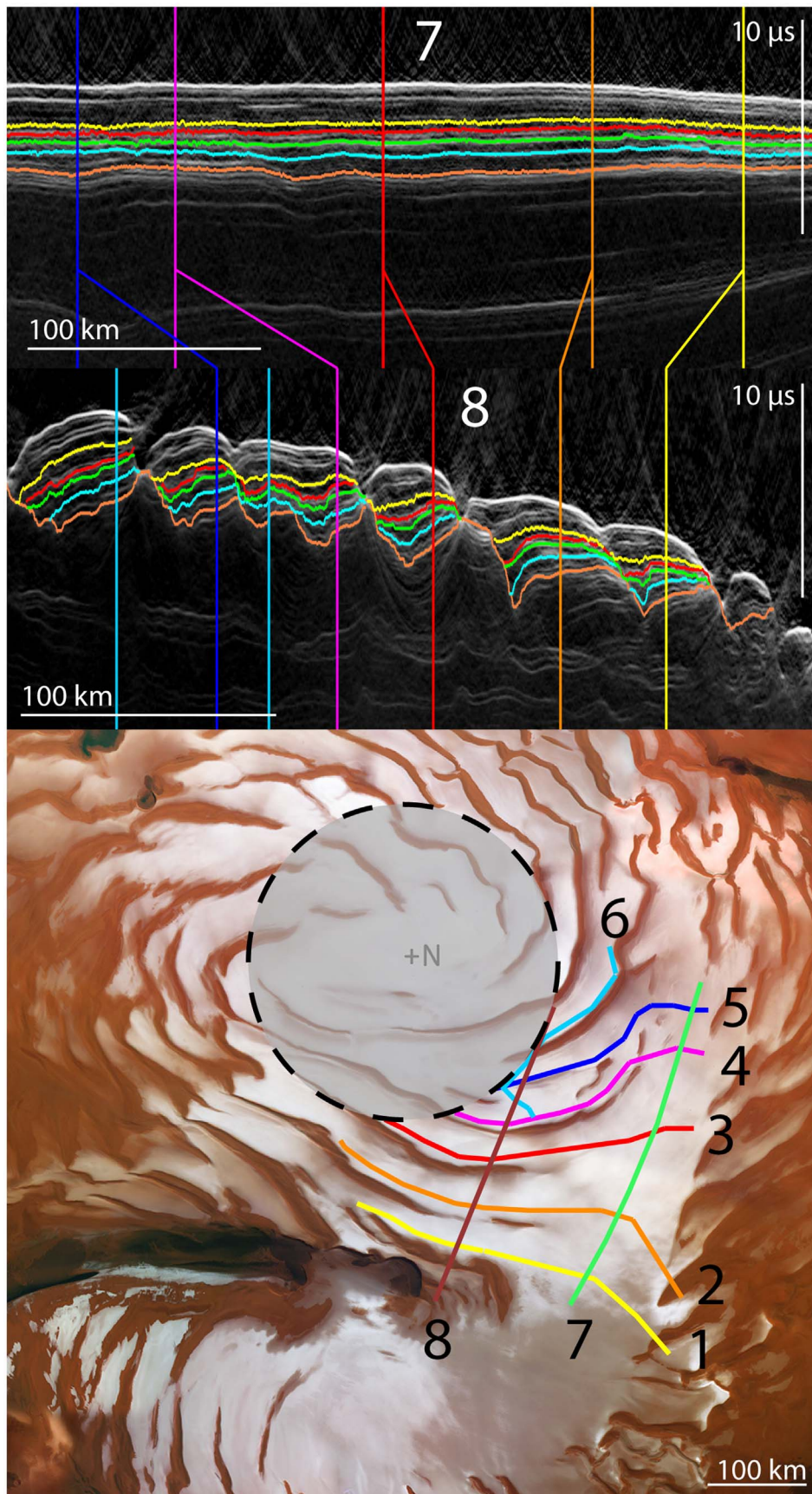


Figure 10. (Continued.)

estimated volume of ice. We consider this result to be within the margin of error for the standard 2D analysis that required interpolation of results between orbit tracks.

In Gemina Lingula, the improved accuracy with which we could track each radar reflector relative to that possible with 2D radargrams and the prior 3D radargram (Figure 9) allowed us to map interfaces that revealed buried structures between layers. We were also able to determine individual layer thicknesses, including those of the entire upper stratigraphic package delineated by five mapped radar reflectors extending to depths of ~600 m. When comparing features in this region between the prior 3D radargram and the new one, we find that distinguishing individual layers and structures is substantially easier in the new data volume.

Similar to previous mapping efforts by Smith & Holt (2015), we are able to demonstrate with the new 3D radargram that the spiral troughs have moved over time. All troughs in our region of interest have moved northward, with a maximum translocation distance of ~70 km in this region. The reflectors used in this mapping are continuous when viewed in profiles parallel to the trough strike but disconnected and vertically offset when viewed in profiles perpendicular to the trough strike. In Figure 10, we demonstrate that all five mapped reflectors are continuous across noncrossing profiles 1–5, and we connected these reflectors via crossing profile 7. Thus, the reflectors in profile 1 can be connected to those at profile 5, even though four spiral trough discontinuities are present between them.

This tracing of reflectors demonstrates that the spatial pattern of deposition is affected by the spiral trough presence. Along profile 7, layer thicknesses vary only by a small amount; however, along profile 8, layers thicken and thin depending on proximity to a spiral trough and from which direction one approaches it. As noted by Smith et al. (2013), the thickest layers are immediately south of each spiral trough, where deposition is greatest. Layer thickness is at a minimum on the north side of the troughs, where erosion removes material and the layers are often visible in outcrops.

Smith et al. (2013) hypothesized that, as katabatic winds descend from the center of the NPLDs during late spring, the winds transport ice (through two phase changes of solid to gas and later from gas to solid) from the sites of ablation to those of deposition. Smith & Holt (2015) demonstrated that the quantity of missing ice at the sites of ablation is similar in magnitude to the quantity of excess ice at the sites of deposition. Our observations support that conclusion. All told, the spiral troughs strongly affect the depositional pattern of ice across the NPLDs through their disruption of uniform accumulation, and locations without troughs (e.g., profile 7) experience very little variability in layer thickness.

4. Discussion

The results presented herein highlight examples of mapping and radar analysis improvements that are possible using PB3Dv2 that we produced from 3399 SHARAD observations acquired from 2006 December through 2019 September. In comparison to a previously generated 3D radargram for the same region, the resolution and clarity of the resulting image are greatly improved. One may discern details of the subsurface structure and features throughout the NPLD and well into the underlying BUs that sit atop the geologic units of the surrounding Vastitas Borealis plains.

Additional work is needed to fully take advantage of this uniquely rich data set, including a thorough mapping of detected interfaces, a full assessment of subsurface structure and stratigraphy, and the identification of buried impact craters. The latter task is complicated by the fact that the 3D migration process may leave artifacts in the form of full or partial hyperboloids of revolution that have circular plan views that could be mistaken for craters (Putzig et al. 2018). Another important caveat with this data volume is that the coverage density of the input data decreases with latitude, which leads to the need for interpolation across coverage gaps in the 3D binning space and a greater density of processing artifacts as one approaches the periphery. Coanalysis using both 2D and 3D radargrams is warranted when assessing outlying areas.

In principle, the methods employed herein may be used anywhere that coverage densities are sufficient to avoid excessive aliasing in the imaging of the surface and subsurface reflections. The most obvious choice for a next application of the method is Planum Australe, for which a first 3D radargram exists that was created using the same methods as those of PB3Dv1. In addition, a pilot study supported by the MRO Project has recently demonstrated that these 3D processing methods are suitable for some mid-latitude sites such as a portion of Deuteronilus Mensae, where debris-covered glaciers are prevalent (Russell et al. 2021). Work is underway to apply these methods for several additional locations in the mid-latitude regions.

We are grateful to NASA, ASI, the MRO Project, and the SHARAD Team for ongoing support of this incredibly successful mission and instrument. We also thank SeisWare for academic licenses to GSW, used in analysis of 2D and 3D radargrams, and Halliburton Landmark for licensing of their ProMAX/SeisSpace™ data processing software, used in the generation of the 3D radargrams. We greatly appreciate positive and constructive comments provided by two anonymous reviewers and the PSJ Data Editor that improved the manuscript. Access to processing tools used to produce the long-aperture 2D radargrams are publicly available via the Colorado Shallow Radar Processing System (CO-SHARPS). CO-SHARPS access instructions and the 3D radargrams are available through the US SHARAD Team's website at <https://sharad.psi.edu>. The original Planum Boreum 3D radargram is also available through the NASA PDS Geosciences node (Putzig et al. 2021), and the new one is in delivery and will be made available online at <https://doi.org/10.17189/a5av-yc11>. This work was supported predominantly by NASA Mars Data Analysis Program grant NNX16AN90G, and additional support in completing this manuscript was provided by the MRO Project. Participation by I.H.M. was made possible through the Jefferson County Colorado High School Executive Internship Program.

ORCID iDs

Nathaniel E. Putzig  <https://orcid.org/0000-0003-4485-6321>
 Bruce A. Campbell  <https://orcid.org/0000-0002-0428-8692>
 Matthew R. Perry  <https://orcid.org/0000-0003-3434-5333>
 Isaac B. Smith  <https://orcid.org/0000-0002-4331-913X>

References

- Biondi, B., Biondi, B. L., Palacharia, G., et al. 2006, in 3D Seismic Imaging (Vol. 14) ed. L. Biondi (Tulsa, OK: Society of Exploration Geophysicists), 51
 Byrne, S. 2009, *AREPS*, 37, 535
 Campbell, B. A., Morgan, G. A., Bernardini, F., et al. 2021, *Icar*, 360, 114358

- Campbell, B. A., & Phillips, R. J. 2014, Mars Reconnaissance Orbiter Shallow Radar Radargram Data, MRO-M-SHARAD-5-RADARGRAM-V1.0, NASA Planetary Data System, doi:[10.17189/1519527](https://doi.org/10.17189/1519527)
- Campbell, B. A., & Phillips, R. J. 2021, Mars Reconnaissance Orbiter Shallow Radar Radargram Data, MRO-M-SHARAD-5-RADARGRAM-V2.0, NASA Planetary Data System, doi:[10.17189/YB1W-F075](https://doi.org/10.17189/YB1W-F075)
- Campbell, B. A., Putzig, N. E., Carter, L. M., & Phillips, R. J. 2011, *IGRSL*, **8**, 939
- Campbell, B. A., Putzig, N. E., Foss, F. J., II, & Phillips, R. J. 2014, *IGRSL*, **11**, 632
- Choudhary, P., Holt, J. W., & Kempf, S. D. 2016, *IGRSL*, **13**, 1285
- Clifford, S. M., Crisp, D., Fisher, D. A., et al. 2000, *Icar*, **144**, 210
- Foss, F. J., Putzig, N. E., Campbell, B. A., & Phillips, R. J. 2017, *The Leading Edge*, **36**, 43
- Grima, C., Kofman, W., Mougnot, J., et al. 2009, *GeoRL*, **36**, L03203
- Holt, J. W., Fishbaugh, K. E., Byrne, S., et al. 2010, *Natur*, **465**, 446
- Levin, S. A., & Foss, F. 2014, in SEG Technical Program Expanded Abstracts 2014 (Tulsa, OK: Society of Exploration Geophysicists), 3821
- Mueller, I., Russell, A. T., Perry, M., & Putzig, N. E. 2021, AGUFM, **P35G–2211**
- Nerozzi, S., & Holt, J. W. 2018, *Icar*, **308**, 128
- Nerozzi, S., & Holt, J. W. 2019, *GeoRL*, **46**, 7278
- Nerozzi, S., Ortiz, M. R., & Holt, J. W. 2022, *Icar*, **373**, 114716
- Neukum, G., Jaumann, R. & The HRSC Co-Investigator and Experiment Team 2004, in ESA SP-1240, Mars Express: The Scientific Payload, ed. A. Wilson & A. Chicarro (Noordwijk: ESA), 17
- Phillips, R. J., Zuber, M. T., Smrekar, S. E., et al. 2008, *Sci*, **320**, 1182
- Putzig, N. E., Foss, F. J., II, Campbell, B. A., Perry, M. R., & Phillips, R. J. 2021, Mars Reconnaissance Orbiter Shallow Radar 3D Data, MRO-M-SHARAD-5-3D-V1.0, NASA Planetary Data System, doi:[10.17189/qk73-zx21](https://doi.org/10.17189/qk73-zx21)
- Putzig, N. E., Phillips, R. J., Campbell, B. A., et al. 2009, *Icar*, **204**, 443
- Putzig, N. E., Smith, I. B., Perry, M. R., et al. 2018, *Icar*, **308**, 138
- Russell, A. T., Bain, Z. M., Perry, M. R., et al. 2021, AGUFM, **P35G–2213**
- Seu, R., Phillips, R. J., Biccari, D., et al. 2007, *JGRE*, **112**, E05S05
- Smith, D., Neumann, G., Arvidson, R. E., Guinness, E. A., & Slavney, S. 2003, Mars Global Surveyor Laser Altimeter Mission Experiment Gridded Data Record, MGS-M-MOLA-5-MEGDR-L3-V1.0, NASA Planetary Data System, doi:[10.17189/1519460](https://doi.org/10.17189/1519460)
- Smith, I. B., Hayne, P. O., Byrne, S., et al. 2020, *P&SS*, **184**, 104841
- Smith, I. B., & Holt, J. W. 2010, *Natur*, **465**, 450
- Smith, I. B., & Holt, J. W. 2015, *JGRE*, **120**, 362
- Smith, I. B., Holt, J. W., Spiga, A., Howard, A. D., & Parker, G. 2013, *JGRE*, **118**, 1835
- Smith, I. B., Putzig, N. E., Holt, J. W., & Phillips, R. J. 2016, *Sci*, **352**, 1075
- Stolt, R. H. 1978, *Geop*, **43**, 23
- Tanaka, K. L., & Fortezzo, C. M. 2012, U.S. Geological Survey Scientific Investigations Map, 3177, USGS, doi:[10.3133/sim3177](https://doi.org/10.3133/sim3177)
- Whitten, J. L., & Campbell, B. A. 2018, *JGRE*, **123**, 1541